

# Ultrafast 4D scanning transmission electron microscopy for imaging of localized optical fields

Petr Koutenský<sup>1,a</sup>, Neli Laštovičková Streshkova<sup>1</sup>, Kamila  
Moriová<sup>1</sup>, Marius Constantin Chirita Mihaila<sup>1</sup>, Alexandr Knápek<sup>2</sup>,  
Daniel Burda<sup>2</sup>, and Martin Kozák<sup>1,b</sup>

<sup>1</sup>Department of Chemical Physics and Optics, Faculty of  
Mathematics and Physics, Charles University, Ke Karlovu 3,  
Prague CZ-12116, Czech Republic.

<sup>2</sup>Institute of Scientific Instruments of the Czech Academy of  
Sciences.

<sup>a</sup>Corresponding authors: petr.koutensky@matfyz.cuni.cz

<sup>b</sup>m.kozak@matfyz.cuni.cz

February 12, 2025

**Ultrafast electron microscopy aims for imaging transient phenomena occurring on nanoscale. One of its goals is to visualize localized optical and plasmonic modes generated by coherent excitation in the vicinity of various types of nanostructures. Such imaging capability**

was enabled by photon-induced near-field optical microscopy, which is based on spectral filtering of electrons inelastically scattered due to the stimulated interaction with the near-field. Here we report on the development of ultrafast 4D scanning transmission electron microscopy, which allows us to image the transverse components of the optical near-field while avoiding the need of electron spectral filtering. We demonstrate that this method is capable of imaging optical near-fields of a tungsten nanotip and ponderomotive potential of an optical standing wave with a spatial resolution of 21 nm.

## 1 Introduction

Electron microscopy has evolved into a versatile tool that provides insight into the nanoworld. Image formation in electron microscopes is mostly based on elastic scattering of electrons on the electrostatic potential of atomic cores while electron spectroscopy relies on inelastic scattering of electrons interacting with shell electrons in the specimen atoms or spontaneously exciting plasmons, phonons or other types of excitations in the studied material. Recent developments have enabled, e.g., to perform vibrational spectroscopy of individual atoms [1, 2] or to visualize complex structure of viruses or proteins [3, 4]. In addition to the ultimate spatial and spectral resolution provided by the state-of-the-art electron microscopes, an insight into ultrafast dynamics occurring on femtosecond to nanosecond time scales has been enabled by combining pulsed laser and electron beams in a pump-probe fashion [5].

One of the fundamental dynamical processes occurring on sub-nanometer spatial scales and femtosecond time scales is light-matter interaction. When a material is illuminated by a light wave, the oscillatory motion of electrons with respect to heavy static ions leads to formation of oscillating dipoles which emit

the electromagnetic field at the frequency of the incident field. In homogeneous materials, this effect gives rise to a refractive index because of the phase delay of the emitted wave, whose interference with the incident wave slows down the phase velocity of light. When the oscillating dipoles are excited in a nanostructure with spatial dimensions smaller than the wavelength of the excitation light field, the superposition of the dipole-like radiation emitted by the nanostructure with the incident wave leads to a local enhancement of the electric field amplitude of the field oscillating at the optical frequency. Such local field enhancement has many applications, for example, surpassing the resolution limit in optical microscopy [6] or enhancing the nonlinear optical interactions driven in metamaterials or individual nanophotonic systems [7–9]. The spatial and spectral distributions of the induced electromagnetic near-fields determine the functionality of nanophotonic devices. However, characterization of the near-field properties often rely on numerical simulations, which typically represent approximate solutions.

Optical near-fields can be experimentally visualized on their natural length and time scales using photon-induced near-field electron microscopy (PINEM) utilizing the electrons inelastically scattered by the interaction with the localized electromagnetic mode to form an image of the near-field distribution. Since its invention [10–13], this technique has been applied for imaging biological structures [14–16], plasmonic excitations [17–20] or optical near-fields of nanostructures [21–23]. The electron-photon coupling can be understood as a harmonic phase modulation at the light frequency imprinted on the electron wave function [11]. In the particle picture, the electron absorbs or emits individual photons of the coherent excitation field in a stimulated manner. Such interaction is prohibited in vacuum due to different dispersion relations of electrons and photons preventing to fulfill the energy and momentum conservation laws. When a

photon is spatially confined at a distance shorter than its wavelength, its momentum becomes delocalized due to Heisenberg uncertainty principle and both the momentum and energy are conserved during inelastic scattering of electrons. Because this process is stimulated, its probability is many orders of magnitude larger than the probability of spontaneous electron energy loss, making PINEM a more sensitive alternative to imaging of the localized photon density of states based on electron energy-loss spectroscopy [15].

Due to a short interaction time of only few femtoseconds in the case of nanostructures with sub-wavelength dimensions, the electron-photon coupling is rather weak and ultrashort optical pulses with high field amplitudes are required to excite the near-fields. Efficiency of coupling between electrons and localized light modes can be enhanced in the vicinity of periodic nanostructures [24–27], in evanescent fields leaking from a dielectric crystal [28, 29] or from an optical cavity [30–32]. Alternatively to optical near-fields, the electrons can inelastically scatter of optical fields generated at thin membranes [33–36] or via the interaction with optical ponderomotive potential in vacuum [37–39]. The PINEM scheme has been modified by adding a second coherent optical interaction allowing to resolve both the amplitude and phase of optical near-fields [40–47]. The instrumentation typically used for PINEM-type imaging involves an ultrafast transmission electron microscope with an electron spectrometer or energy filter. In this configuration, the technique is sensitive only to the component of the electric field along the direction of propagation of electrons [10, 11]. Because the resulting image does not contain direct information about the local electric field but rather about the total electron momentum change corresponding to the field integrated over the interaction distance, it is not possible to reconstruct the full 3D vectorial electromagnetic field from these images.

Here we propose and demonstrate a novel approach as an alternative to



PINEM, enabling the visualization of the interaction between electrons and optical fields in electron microscopes without the need for an electron spectrometer. The method is based on ultrafast 4D scanning transmission electron microscopy (U4DSTEM, experimental setup is shown in Fig. 1a, details can be found in Methods, section Experimental setup), by which we monitor the deflection of low-energy electrons (20 keV) due to the interaction with localized optical fields or with ponderomotive potential of an optical standing wave as a function of beam position in the sample plane. By processing the scattered electron images obtained while scanning the electron beam across the sample we obtain information about the strength and direction of the Lorentz force acting on the electron during the interaction with the optical fields.

The interaction between an electron and electromagnetic fields in vacuum can be described classically, semi-classically, or by a fully quantum approach. The PINEM experiments usually occur in the regime in which the initial electron spectrum is narrower than the photon energy of the excitation. In such a case, the electron coherence time is longer than one temporal period of the oscillating field of the excitation and quantum mechanical interference effects may be expected in the final spectrum. These manifest themselves as discrete peaks separated by the photon energy of the excitation [10, 21]. When applying the semi-classical (light is treated classically, electron is described as a wavepacket) and non-recoil (negligible change of electron momentum) approximations, the inelastic electron scattering is a result of time-dependent phase modulation imprinted to the electron wave function. The additional phase acquired by the electron during the interaction with optical fields can be written as [48]:

$$\Phi(\mathbf{r}, t) = -\frac{1}{\hbar} \int_{t_0}^t \hat{\mathbf{H}}_{\text{int}}[\mathbf{r}(t'), t'] dt', \quad (1)$$

where  $\hat{\mathbf{H}}_{\text{int}}[\mathbf{r}(t'), t'] = \{\hat{\mathbf{p}} + e\mathbf{A}[\mathbf{r}(t')]\}^2/(2m)$  is the interaction Hamilto-

nian of an electron with charge  $e$  and mass  $m$  interacting with the electromagnetic field with vector potential  $\mathbf{A}(\mathbf{r}, t)$  in vacuum and  $\mathbf{r}(t')$  is the unperturbed classical trajectory of the electron. The coupling between an electron and the electromagnetic field is described by two terms in  $\hat{\mathbf{H}}_{\text{int}}$ . The PINEM-type interaction is described by a term linear in the field strength  $\approx \mathbf{p}_0 \cdot \mathbf{A}(\mathbf{r}, t)$ , where  $\mathbf{p}_0 = (0, 0, p_z)$  is the initial electron momentum and  $\mathbf{A}(\mathbf{r}, t)$  is the vector potential. The second term responsible for phase modulation of the electron wave is the ponderomotive term  $\approx |\mathbf{A}(\mathbf{r}, t)|^2$ , which becomes important when the interaction occurs in vacuum. When we focus on the former case of linear coupling, the scalar product between the initial electron momentum and the vector potential suggests that only the longitudinal momentum component of the electron is modulated. However, in the optical near-field region, the amplitude of the vector potential changes rapidly in the transverse direction in the  $x - y$  plane leading to a transverse dependence of the interaction strength. As a consequence, electron phase fronts become tilted with respect to the planar phase fronts of the initial electron wave and the tilt depends on the phase of the oscillating vector potential, which the electron experiences (see Fig. 1b). The tilted electron waves are deflected in the transverse plane and form a scattered electron image at the detector.

We note that there is one significant difference between the final transverse and longitudinal electron momentum distributions after the interaction with the optical fields. When we consider a strongly localized optical near-field, the electron wave feels periodic oscillations of the vector potential when traveling through. The periodicity of the field in the time domain translates to the periodic phase modulation of the electron wavefunction in the direction of electron propagation when expressed in the electron's rest frame  $z' = z - vt$ . It is this periodicity in space and time that leads to the discrete peaks in the longitudinal

electron momentum and its kinetic energy spectra. When such periodicity is missing in the transverse spatial direction, no separated peaks are expected in the electron transverse momentum spectra. We come to the same conclusion when considering the particle picture of the interaction. When photons are localized in the transverse direction at a much smaller spatial scale than the wavelength of the exciting light, they become strongly delocalized in the transverse momentum space. The localization of the field in the  $z$ -direction in the laboratory frame is removed in the electron's rest frame allowing the appearance of the discrete peaks in the energy and longitudinal momentum spectra.

Since no quantum-mechanical effects are to be expected in the transverse electron distribution in the case of localized non-periodic near-fields, we can describe the interaction of the electrons within classical approximation in the electron rest frame, where the  $j$  component of the total change of electron transverse momentum at spatial coordinates  $x, y$  can be expressed as:

$$\Delta p_j(x, y) = \int_{-\infty}^{\infty} F_j(x, y, t) dt, \quad (2)$$

where  $F_j = e[\mathbf{E} + (\mathbf{v} \times \mathbf{B})]_j$  denotes the  $j$ -th component of the Lorentz force with the electric and magnetic fields  $\mathbf{E} = \Re \left\{ \tilde{\mathbf{E}}(\mathbf{r}, \omega) g(t - \Delta t) e^{i\omega t + i\varphi_0} \right\}$  and  $\mathbf{B} = \Re \left\{ \tilde{\mathbf{B}}(\mathbf{r}, \omega) g(t - \Delta t) e^{i\omega t + i\varphi_0} \right\}$ , respectively. Here  $\Delta t$  represents the electron arrival time and  $g(t - \Delta t)$  and  $\varphi_0$  are the envelope and phase of the optical fields, respectively. The spatial distributions of the electromagnetic fields  $\tilde{\mathbf{E}}(\mathbf{r}, \omega)$  and  $\tilde{\mathbf{B}}(\mathbf{r}, \omega)$  at frequency  $\omega$  are obtained from a numerical solution of Maxwell's equations (for details see Methods, section Numerical simulations). The electric and magnetic fields are in the case of quasimonochromatic pulses related to the vector potential via  $\mathbf{E} = -\partial \mathbf{A} / \partial t$  (we assume constant electrostatic potential corresponding to zero electrostatic field) and  $\mathbf{B} = \nabla \times \mathbf{A}$ . When describing the interaction of electrons with the ponderomotive potential

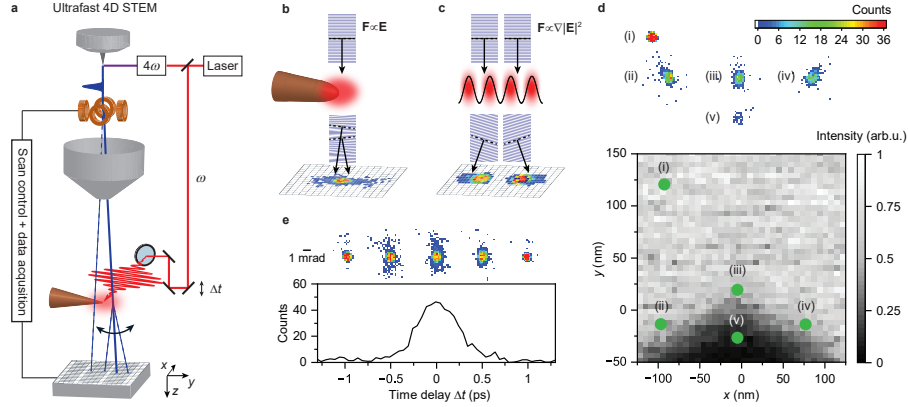


Figure 1: **Ultrafast 4D scanning transmission electron microscopy (U4DSTEM)**. **a**, Layout of the U4DSTEM experimental setup. **b**, **c**, Illustration of electron phase-fronts in  $y - z$  plane in the case of the interaction with **b** a localized optical near-field and **c** the ponderomotive potential of an optical standing wave. **d**, Grey scale: scanning transmission electron image of the tungsten nanotip. Color scale shows the measured electron scattering patterns in five points labeled as (i)-(v). **e**, Evolution of the number of electrons elastically scattered by the interaction with the optical near-field of a nanotip as a function of the mutual time delay  $\Delta t$  between electron and light pulses. Color scale shows the electron scattering patterns measured with different  $\Delta t$ .

in vacuum, the Lorentz force can be integrated over the optical cycle to give the nonrelativistic ponderomotive force  $F_j = -e^2/(4m\omega^2)\nabla_j \langle |\mathbf{E}|^2 \rangle$ .

## 2 Results

### 2.1 Imaging of optical near-field of a tungsten nanotip

U4DSTEM principle is demonstrated on two model examples. In the first example, we image the transverse component of the optical near-field generated by coherent excitation on the surface of a tungsten nanotip (for details on preparation of the nanotips see Methods, section Preparation of nanotips). The layout of the experimental setup is shown in Fig. (1a). A pulsed laser beam with a wavelength of 1030 nm and a pulse duration of 250 fs is incident to the nan-

otip from the direction perpendicular to the plane defined by the tip symmetry axis and the propagation direction of the electron beam. The excitation light is linearly polarized along the nanotip symmetry axis. The pulsed electron beam with a kinetic energy of 20 keV, repetition rate of 500 kHz and a pulse duration of 500 fs, is focused on the nanotip situated in a working distance of the electron microscope of 11.5 mm. To generate an almost collimated electron beam with a current sufficient for U4DSTEM imaging, we use the highest probe current setting of the electron microscope. The beam divergence is reduced by introducing an objective lens aperture with a diameter of 64  $\mu\text{m}$ . The resulting electron beam has a spot size in focus of 21 nm and a divergence angle of 1.3 mrad.

The strength of the transverse component of the Lorentz force acting on the electrons is measured as a function of the position of the electron beam in the sample plane by detecting the scattered electron images. In Fig. (1d) we show the bright-field scanning transmission electron microscopy (STEM) image of the nanotip apex with five selected positions of the electron beam labeled (i)-(v). The images detected by the pixel detector in each of these positions are shown in the upper part of Fig. (1d). We observe that the electrons are scattered in the transverse direction by the interaction with the optical near-field. The scattered images carry information about the strength and the direction of the Lorentz force (the main axis of the ellipse rotates according to the preferential polarization of the electric component of the near-field).

To rule out a significant contribution from elastic electron scattering caused directly by the nanotip surface, we measure the electron scattering patterns as a function of the time delay  $\Delta t$  between the electron and laser pulses with the electron beam position fixed in the spot (iii). The measured population of scattered electrons is shown in Fig. (1e) as a function of  $\Delta t$  (black curve) along with the scattered electron images in five selected time delays (color scale).

The data clearly show that electron deflection is observed only when the two pulses arrive at the nanotip at the same time, confirming that elastic electron scattering originates from the interaction with the optical near-field instead of the interaction with the nanotip itself.

The transverse components of the near-field are obtained by processing the U4DSTEM data measured at the optimal time overlap between the electron and light pulses. Because the electrons arrive to the sample at different times within the pulse envelope, they experience different amplitude and phase of the oscillating near-field, which is generated by a femtosecond optical pulse. The maximum transverse momentum change of the electrons corresponding to the amplitude of the Lorentz force can be obtained by analyzing the maximum electron deflection in the particular beam position in the sample plane. However, because of the small amount of electrons detected per pixel, the image processing by fitting the streaked electron images exhibits high noise.

For this reason, we apply an alternative data processing method in which we first numerically determine the function describing the relation between the maximum of the Lorentz force and the total number of electrons deflected out of the detector region illuminated by the undeflected electron beam. The maximum change in transverse momentum of the electrons  $\Delta p_{\perp}$  in each position on the sample is then determined purely by counting the deflected electrons. The azimuthal angle  $\alpha$  of the maximum of the Lorentz force acting on the electrons in the  $x - y$  plane is obtained by fitting each image of the scattered electrons by a 2D Gaussian function and determining the direction of its main axis. The  $x$  and  $y$  components of  $\Delta p_{\perp}$  are then  $\Delta p_x = \Delta p_{\perp} \cos(\alpha)$  and  $\Delta p_y = \Delta p_{\perp} \sin(\alpha)$  (details of data processing are described in Methods, section Data acquisition and processing). The measured spatial maps of  $\Delta p_x$  and  $\Delta p_y$  are shown in Fig. (2a,b) compared to the numerical simulations shown in Fig. (2)c,d. The

amplitude of the measured transverse momentum change of the electrons allows us to estimate the maximum electric field amplitude at the tip surface to be  $E_y^{\max} = 3.1 \pm 0.3$  GV/m. The uncertainty was estimated based on the fact that we only exactly know the shape of the  $x - y$  projection of the tip while the electron deflection is influenced by the extension of the field in  $z$  direction. The amplitude of the electric field of the excitation pulse in the experiments is  $E_0 = 0.7 \pm 0.05$  GV/m giving the field enhancement factor of  $\xi_{\text{exp}} = 4.4 \pm 0.5$  [49], which agrees well with the value of  $\xi_{\text{sim}} = 4.55$  obtained using numerical simulations (for details see Methods, section Numerical simulations). In Fig. (2)e we compare the measured (black curve) and numerically calculated (red curve) spatial decay of the transverse momentum change of the electrons  $\Delta p_y$  obtained by integrating the data in the region of Fig. (2)a,b labeled by the dashed lines. Bright-field STEM images of the nanotip measured with the pulsed electron beam are used to determine the spatial resolution of the method, which is 21 nm in this experiment. In Fig. (2)f we show an image of the amplitude of the optical near-field by measuring the maximum of the total transverse momentum change of the electrons  $\Delta p_{\perp}$  induced by the near-field of a blunter tip with a larger radius of curvature of the apex. From the smaller value of the observed momentum change close to the tip apex and from the fact that the interaction time increases in the case of the blunter tip, we can deduce that the field enhancement is smaller compared to the case shown in Fig. (2)a.

## 2.2 Imaging of an optical standing wave

In addition, we demonstrate the capabilities of U4DSTEM imaging for visualization of the ponderomotive potential of optical fields in vacuum. For this purpose, we generate an optical standing wave by two counter-propagating pulsed light beams of the same frequency  $\omega$ . The time-averaged intensity of the electric field

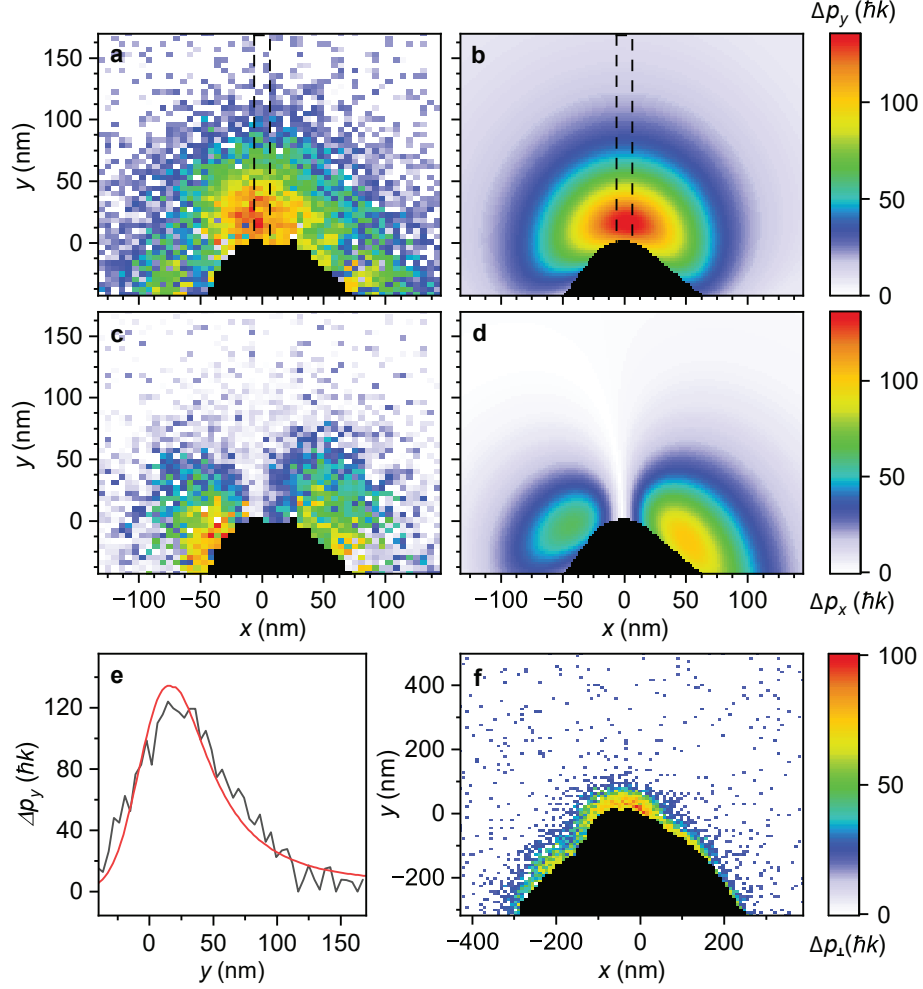


Figure 2: **Imaging of the transverse component of Lorentz force of optical near-field generated on the surface of a tungsten nanotip by coherent optical excitation.** **a**, Maximum of the measured  $y$ -component of the transverse momentum change of the electrons  $\Delta p_y$  and its  $x$ -component  $\Delta p_x$  (**c**) compared to the numerical results shown in **b**, **d**. **e**, Comparison of the measured (black curve) and the calculated (red curve) spatial profiles of  $\Delta p_y$  obtained by integrating the in the region marked by dashed lines in **a** and **b**. **f**, Maximum of the total transverse momentum change of the electrons  $\Delta p_{\perp}$  induced by the near-field of a blunter tip with larger radius of curvature of the apex.



can be written as:

$$\langle |\mathbf{E}(\mathbf{r}, t)|^2 \rangle = 2E_0^2 [1 + \cos(2k_x x)] G(\mathbf{r}, t), \quad (3)$$

where  $E_0$  is the electric field amplitude of each of the two pulses,  $k_x = \omega/c$  is the length of the wave vector corresponding to the optical field forming the standing wave and  $G(\mathbf{r}, t)$  is the spatio-temporal envelope of the optical beams. The quiver motion of the electrons in the oscillating electromagnetic field of light generates ponderomotive potential. The gradient of the potential expressed by Eq. (3) along the transverse directions with respect to the electron beam gives an effective force with nonrelativistic expression [50]:

$$\mathbf{F}(\mathbf{r}, t) = -\frac{e^2}{4m_0\omega^2} \nabla \langle |\mathbf{E}(\mathbf{r}, t)|^2 \rangle = \left[ 0, \frac{e^2 E_0^2 k_x G(\mathbf{r}, t)}{m_0\omega^2} \sin(2k_x x), 0 \right], \quad (4)$$

where we assume a slowly-varying envelope approximation  $|\nabla G(\mathbf{r}, t)| \ll |k_x G(\mathbf{r}, t)|$ . The U4DSTEM image of the optical standing wave is shown in Fig. (3)a,b, where we plot the maximum electron momentum change  $\Delta p_x$  as a function of the electron beam position in the sample plane. Due to the high gradient of the optical intensity in  $x$ -direction, the electrons are deflected depending on their position with respect to the standing wave. From the maximum measured momentum change  $\Delta p_x$  corresponding to the trajectories of electrons deflected by the largest angles we estimate the peak intensity of the optical standing wave to be  $6.52 \text{ TW} \cdot \text{cm}^{-2}$  (see Methods, section Data processing - imaging of the optical standing wave for details).

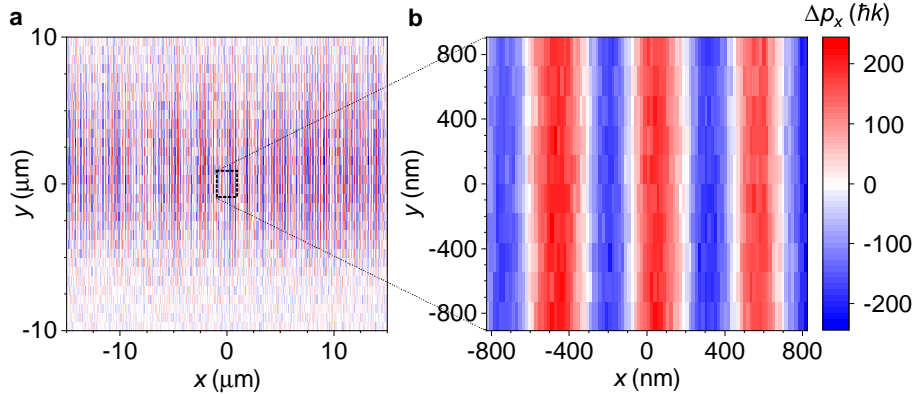


Figure 3: **Imaging of ponderomotive potential of an optical standing wave in vacuum.** **a**, Color scale shows the maximum electron momentum change  $\Delta p_x$  as a function of the electron beam position in the sample plane. **b**, Detail of the image shown in **a**.

### 3 Discussion and conclusions

The sensitivity of U4DSTEM imaging is limited by the minimum electron beam deflection angle, which can be measured. For our experimental conditions, this limit is posed by the angular size of individual detector pixels, which is 0.33 mrad. The corresponding minimum electric field amplitude that can be detected is  $E \approx 1 \text{ GV/m}$ . The detection sensitivity may be further influenced by elastic electron scattering from the sample itself and by the background signal coming from the excitation light scattered to the detector. Although hybrid pixel detectors are not sensitive to individual low-energy photons, when the nanostructure is excited by a femtosecond optical pulse with high peak intensity, many scattered photons can be incident on each pixel within a detection time window of a few nanoseconds. The background optical signal can be avoided by deflecting the electrons by a weak electric or magnetic field and blocking the photons incident on the detector.

The spatial resolution of U4DSTEM may be improved in the future by implementing higher repetition rates allowing to generate a highly collimated pulsed

electron beam with smaller spot size while keeping the average electron current at the same level. In principle, the method is also suitable for imaging continuous evanescent fields of resonant structure where absorption/emission of several hundreds of photons by a single electron has been demonstrated in classical PINEM experiments [32].

In conclusion, the U4DSTEM represents an alternative technique to PINEM, which allows us to image the transverse component of the optical near-field excited in the vicinity of a metallic nanotip by coherent optical radiation and the ponderomotive potential of an optical standing wave. U4DSTEM can be utilized to image the local density of optical modes of various types of nanophotonic and plasmonic structures, metamaterials or photonic crystals. Combined with the possibility of tuning the frequency of coherent optical excitation, this technique may provide spectral resolution similar to electron energy gain spectroscopy [51]. It offers two significant advantages compared to PINEM. First, it does not require an electron spectrometer, which together with a suitable electron detector represents significant costs in ultrafast electron microscope setup. Second, the U4DSTEM technique can be implemented in low-energy scanning electron microscopes, making it more accessible to users.

## 4 Acknowledgments

The authors acknowledge funding from the Czech Science Foundation (project 22-13001K), Charles University (SVV-2023-260720, PRIMUS/19/SCI/05, GAUK 90424) and the European Union (ERC, eWaveShaper, 101039339). Views and opinions expressed are however those of the author(s) only and do not necessarily reflect those of the European Union or the European Research Council Executive Agency. Neither the European Union nor the granting authority can be held responsible for them. This work was supported by TERAFFIT project No.

CZ.02.01.01/00/22\_008/0004594 funded by OP JAK, call Excellent Research.

## References

- [1] Krivanek, O. *et al.* Vibrational spectroscopy in the electron microscope. *Nature* **514**, 209–212 (2014).
- [2] Hage, F. S., Radtke, G., Kepaptsoglou, D. M., Lazzeri, M. & Ramasse, Q. M. Single-atom vibrational spectroscopy in the scanning transmission electron microscope. *Science* **367**, 1124–1127 (2020).
- [3] Sirohi, D. *et al.* The 3.8 Å resolution cryo-EM structure of Zika virus. *Science* **352**, 467–470 (2016).
- [4] Cheng, Y. Single-particle cryo-EM—How did it get here and where will it go. *Science* **361**, 876–880 (2018).
- [5] Zewail, A. H. & Thomas., J. M. *D Electron Microscopy. Imaging in Space and Time*. ISBN: 978-1-908978-43-1 (Imperial College Press, 2009).
- [6] Ash, E. A. & Nicholls, G. Super-resolution aperture scanning microscope. *Nature* **237**, 510–512 (1972).
- [7] Hommelhoff, P., Kealhofer, C. & Kasevich, M. A. Ultrafast electron pulses from a tungsten tip triggered by low-power femtosecond laser pulses. *Phys. Rev. Lett.* **97**, 247402 (2006).
- [8] Ropers, C., Solli, D. R., Schulz, C. P., Lienau, C. & Elsaesser, T. Localized multiphoton emission of femtosecond electron pulses from metal nanotips. *Phys. Rev. Lett.* **98**, 043907 (2007).
- [9] Krasnok, A., Tymchenko, M. & Alù, A. Nonlinear metasurfaces: a paradigm shift in nonlinear optics. *Materials Today* **21**, 8–21 (2018).

- [10] Barwick, B., Flannigan, D. & Zewail, A. H. Photon-induced near-field electron microscopy. *Nature* **462**, 902–6 (2009).
- [11] Park, S. T., Lin, M. & Zewail, A. H. Photon-induced near-field electron microscopy (PINEM): theoretical and experimental. *New J. Phys.* **12**, 123028 (2010).
- [12] García de Abajo, F. J., Asenjo-Garcia, A. & Kociak, M. Multiphoton absorption and emission by interaction of swift electrons with evanescent light fields. *Nano Lett.* **10**, 1859–1863 (2010).
- [13] García de Abajo, F. J. Optical excitations in electron microscopy. *Rev. Mod. Phys.* **82**, 209–275 (2010).
- [14] Flannigan, D. J., Barwick, B. & Zewail, A. H. Biological imaging with 4D ultrafast electron microscopy. *Proc. Natl. Acad. Sci. U. S. A.* **107**, 9933–9937 (2010).
- [15] Vanacore, G., Fitzpatrick, A. & Zewail, A. H. Four-dimensional electron microscopy: Ultrafast imaging, diffraction and spectroscopy in materials science and biology. *Nano Today* **11**, 228–249 (2016).
- [16] Lu, Y. *et al.*. 4D electron microscopy of T cell activation. *Proc. Natl. Acad. Sci. U. S. A.* **116** (2019).
- [17] Piazza, L. *et al.*. Simultaneous observation of the quantization and the interference pattern of a plasmonic near-field. *Nat. Commun.* **6**, 6407 (2015).
- [18] Liu, H., Baskin, J. & Zewail, A. H. Infrared PINEM developed by diffraction in 4D UEM. *Proc. Natl. Acad. Sci. U. S. A.* **113**, 2041–2046 (2016).
- [19] Vanacore, G. M. *et al.*. Ultrafast generation and control of an electron vortex beam via chiral plasmonic near fields. *Nature Materials* **18**, 573–579 (2019).

- [20] Liu, H. *et al.*. Visualization of plasmonic couplings using ultrafast electron microscopy. *Nano Lett.* **21**, 5842–5849 (2021).
- [21] Feist, A. *et al.*. Quantum coherent optical phase modulation in an ultrafast transmission electron microscope. *Nature* **521**, 200–203 (2015).
- [22] Li, H. & Su, Z. Energy-filtered dark-field imaging of nanoparticles by PINEM in 4D electron microscopy. *Appl. Phys. Lett.* **120**, 191103 (2022).
- [23] Shiloh, R., Chlouba, T. & Hommelhoff, P. Quantum-coherent light-electron interaction in a scanning electron microscope. *Phys. Rev. Lett.* **128**, 235301 (2022).
- [24] Breuer, J. & Hommelhoff, P. Laser-based acceleration of nonrelativistic electrons at a dielectric structure. *Phys. Rev. Lett.* **111**, 134803 (2013).
- [25] Harvey, T. R. *et al.*. Probing chirality with inelastic electron-light scattering. *Nano Lett.* **20**, 4377–4383 (2020).
- [26] Shiloh, R. *et al.*. Electron phase-space control in photonic chip-based particle acceleration. *Nature* **597**, 498–502 (2021).
- [27] Chlouba, T. *et al.*. Coherent nanophotonic electron accelerator. *Nature* **622**, 476–480 (2023).
- [28] Kozák, M. *et al.*. Acceleration of sub-relativistic electrons with an evanescent optical wave at a planar interface. *Opt. Express* **25**, 19195–19204 (2017).
- [29] Dahan, R. *et al.*. Resonant phase-matching between a light wave and a free-electron wavefunction. *Nat. Phys.* **16**, 1123–1131 (2020).
- [30] Wang, K. *et al.*. Coherent interaction between free electrons and a photonic cavity. *Nature* **582**, 50–54 (2020).

- [31] Kfir, O. *et al.*. Controlling free electrons with optical whispering-gallery modes. *Nature* **582**, 46–49 (2020).
- [32] Henke, J.-W. *et al.*. Integrated photonics enables continuous-beam electron phase modulation. *Nature* **600**, 653–658 (2021).
- [33] Kirchner, F., Gliserin, A., Krausz, F. & Baum, P. Laser streaking of free electrons at 25 keV. *Nat. Photonics* **8**, 52–57 (2014).
- [34] Morimoto, Y. & Baum, P. Diffraction and microscopy with attosecond electron pulse trains. *Nat. Phys.* **14**, 252–256 (2018).
- [35] Morimoto, Y. & Baum, P. Attosecond control of electron beams at dielectric and absorbing membranes. *Phys. Rev. A* **97**, 033815 (2018).
- [36] Vanacore, G. M. *et al.*. Attosecond coherent control of free-electron wave functions using semi-infinite light fields. *Nat. Commun.* **9**, 2694 (2018).
- [37] Kozák, M., Eckstein, T., Schönenberger, N. & Hommelhoff, P. Inelastic ponderomotive scattering of electrons at a high-intensity optical travelling wave in vacuum. *Nat. Phys.* **14**, 121–125 (2018).
- [38] Kozák, M., Schönenberger, N. & Hommelhoff, P. Ponderomotive generation and detection of attosecond free-electron pulse trains. *Phys. Rev. Lett.* **120**, 103203 (2018).
- [39] Tsarev, M., Thurner, J. W. & Baum, P. Nonlinear-optical quantum control of free-electron matter waves. *Nat. Phys.* **19**, 1350–1354 (2023).
- [40] Echterkamp, K. E., Feist, A., Schäfer, S. & Ropers, C. Ramsey-type phase control of free-electron beams. *Nat. Phys.* **12**, 1000–1004 (2016).
- [41] Kozák, M. *et al.*. Optical gating and streaking of free electrons with sub-optical cycle precision. *Nat. Commun.* **8**, 14342 (2017).

- [42] Priebe, K. E. *et al.*. Attosecond electron pulse trains and quantum state reconstruction in ultrafast transmission electron microscopy. *Nat. Photonics* **11**, 793–797 (2017).
- [43] Ryabov, A., Thurner, J. W., Nabben, D., Tsarev, M. V. & Baum, P. Attosecond metrology in a continuous-beam transmission electron microscope. *Science Advances* **6**, eabb1393 (2020).
- [44] Nabben, D., Kuttruff, J., Stolz, L., Ryabov, A. & Baum, P. Attosecond electron microscopy of sub-cycle optical dynamics. *Nature* **619**, 63–67 (2023).
- [45] Bucher, T. *et al.*. Free-electron Ramsey-type interferometry for enhanced amplitude and phase imaging of nearfields. *Science Advances* **9**, eadi5729 (2023).
- [46] Gaida, J. H. *et al.*. Lorentz microscopy of optical fields. *Nat. Commun.* **14**, 6545 (2023).
- [47] Gaida, J. H. *et al.*. Attosecond electron microscopy by free-electron homodyne detection. *Nat. Photonics* **18**, 509–515 (2024).
- [48] García de Abajo, F. J. & Konečná, A. Optical Modulation of Electron Beams in Free Space. *Phys. Rev. Lett.* **126**, 123901 (2021).
- [49] Krüger, M., Lemell, Ch., Wachter, G., Burgdörfer, J., & Hommelhoff, P. Polarization-dependent ponderomotive gradient force in a standing wave. *J. Phys. B: At. Mol. Opt. Phys.* **51**, 172001 (2018).
- [50] Smorenburg, P. W. *et al.*. Polarization-dependent ponderomotive gradient force in a standing wave. *Phys. Rev. A* **83**, 063810 (2011).
- [51] García de Abajo, F. J., & Kociak, M. Electron energy-gain spectroscopy. *New J. Phys.* **10**, 073035 (2008).



- [52] Knápek, A., Sýkora, J., Chlumská, J. & Sobola, D. Programmable set-up for electrochemical preparation of STM tips and ultra-sharp field emission cathodes. *Microelectronic Engineering* **173**, 42–47 (2017).
- [53] Koutenský, P. *et al.*. Data for "Ultrafast 4D scanning transmission electron microscopy for imaging of localized optical fields". *Zenodo*, DOI: 10.5281/zenodo.14824588.

## 5 Methods

### 5.1 Experimental setup

The experimental setup is shown in Fig. (1.A). The electron-light interactions are studied in a scanning electron microscope Verios 5 UC (Thermo Fisher Scientific), which is modified for ultrafast operation. The electrons are photoemitted from the Schottky-type source using ultraviolet femtosecond laser pulses at the wavelength of 257 nm generated using the fourth harmonic generation of the output of Ytterbium-60 HE (AFS) femtosecond laser system with central wavelength of 1030 nm, pulse duration of 250 fs and repetition rate of 500 kHz. The fundamental output of the laser is used to excite the optical near-fields and to generate the optical standing wave inside the vacuum chamber of the microscope. All experiments are performed with electron kinetic energy of 20 keV. To allow sufficient transverse momentum resolution, we use the microscope setting that generates a beam with a low divergence angle of 1.3 mrad using the highest current settings and introducing an objective aperture with diameter of 64  $\mu\text{m}$ . Each electron pulse contains approximately 0.038 electrons on average, as calculated from the laser repetition rate, exposure time, and number of detected electrons. The duration of the electron pulse in the sample plane was 520 fs (FWHM), see Fig. (1e). The working distance is set to 11.5 mm. The spatial

resolution of U4DSTEM of 21 nm is determined from the 35% – 65% contrast change in the bright-field STEM image of the nanotip, which is fitted by the error function.

The Gaussian width of the focus was  $w_0 = (25 \pm 1) \mu\text{m}$  (FWHM) in the experiment with the nanotip and  $w_0 = (8.8 \pm 0.1) \mu\text{m}$  in the experiment with the optical standing wave. The laser spot size is measured by scanning the nanotip through the laser focus and detecting scattered light. The time delay between the electron pulse and optical fields in the sample plane is controlled using an optical delay line (two independent delay lines are used in the experiment with the optical standing wave). The intensity of excitation is controlled by a combination of a half-wave plate and a polarizer for both the fundamental and the photoemission beams. The electron detector (hybrid pixel detector Timepix3, Advascope) is placed at a distance of  $L = 16.7$  cm downstream of the sample plane. The acquisition of detector data is synchronized with the position of the electron beam in the sample plane, which is controlled externally using a PCIe-6323 card from National Instruments.

## 5.2 Preparation of nanotips

The preparation of sharp tungsten tips using the drop-off method on a polycrystalline tungsten wire with a diameter of 0.3 mm is based on the general technique of anodic dissolution [52]. The method comprises two etching phases: in the first phase, a narrowing of the tungsten wire, referred to as the meniscus, is formed. In the second phase, the tip is etched within a precisely defined region of this narrowing. Several variables influence the etching process, including the applied DC voltage, the type and concentration of the electrolyte (commonly a 8–10% NaOH solution) and the method’s control parameters, such as the current limits set for each phase and the immersion depth of the wire below the

electrolyte surface.

Since etching occurs preferentially where the liquid’s surface tension exerts force on the wire, this method allows direct control over the meniscus region where the tip will be refined in the second phase. At the end of the second phase, the etching source is disconnected immediately after the bottom part of the meniscus drops off, based on the monitoring the second derivative of the electric current, to prevent tip blunting. This approach produces tips with diameters that typically range between 70 and 140 nm.

### 5.3 Data acquisition and processing

In the experiments, the pulsed electron beam is scanned across the sample and an image is taken on the detector placed downstream the sample. Fig. (1d) illustrates typical experimental data in the case of the interaction with optical near-field. The images shown in Fig. 2a,c,f are measured with an acquisition time of 0.2 s per pixel, which gives the total measurement time of about 10 minutes for Fig. 2a,c and 35 minutes for 2f (including readout time). In the classical point-particle approximation, the Lorentz force of the optical near-field deflects the electrons depending on the amplitude and phase of the oscillating field, which the electron experiences. The transverse momentum change of the electron  $\Delta p_{\perp}$  depends on the phase of the optical field  $\varphi_0$  and on the actual amplitude of the laser pulse envelope  $g(\Delta t - t_0)$  during the interaction. Because the electrons are normally distributed within the electron pulse envelope, which is longer than the envelope of the laser pulse exciting the near-field and significantly longer than its cycle, the electrons experience a broad range of interaction strengths. As a result, the electrons scatter and form an elliptically smeared pattern on the detector, which we use to calculate the maximum transverse momentum change of the electrons as a function of the beam position in

the sample plane.

The local direction and amplitude of the electron momentum change is extracted from the measured data by the following procedure. First, we filter out the electrons detected in the region of the primary beam and take into account only the electrons deflected out of this region. We note that we do not observe any motion of the primary beam on the detector with the U4DSTEM field of view of a few hundreds of nanometers. The azimuthal angle  $\alpha$  of the electron deflection in the  $x - y$  plane is obtained by fitting the detected elliptical pattern with a 2D Gaussian function:

$$\begin{aligned}
 f(x_{\text{det}}, y_{\text{det}}, \alpha) &= A \exp(-ax_{\text{det}}^2 - 2bx_{\text{det}}y_{\text{det}} - cy_{\text{det}}^2), \\
 a &= \frac{\cos^2(\alpha)}{2\sigma_1^2} + \frac{\sin^2(\alpha)}{2\sigma_2^2}, \\
 b &= -\frac{\sin(\alpha)\cos(\alpha)}{2\sigma_1^2} + \frac{\sin(\alpha)\cos(\alpha)}{2\sigma_2^2}, \\
 c &= \frac{\sin^2(\alpha)}{2\sigma_1^2} + \frac{\cos^2(\alpha)}{2\sigma_2^2},
 \end{aligned} \tag{5}$$

where  $x_{\text{det}}$  and  $y_{\text{det}}$  are coordinates in the detector plane,  $\sigma_1$  and  $\sigma_2$  are the widths of the main and the secondary axis ( $\sigma_1 > \sigma_2$ ), respectively, and  $\alpha$  is the angle of rotation of the 2D Gaussian in the plane  $x_{\text{det}} - y_{\text{det}}$  plane. The coordinate system is centered in the center of the electron beam on the detector. Because this function does not exactly describe the expected shape of the detected pattern, it is only used to determine the angle of the maximum momentum change  $\alpha$ . To determine the amplitude of the induced transverse momentum change, we first perform numerical simulations of the interaction by calculating the 3D distribution of optical near-field of a tungsten nanotip using a commercial finite-difference time-domain (FDTD) solver Lumerical FDTD. In the simulations we take into account the divergence and 3D envelopes of the electron pulse and the time envelope of the laser pulse used to excite the near-field. From the

calculated distribution of the scattered electrons we determine the theoretical dependence of the number of electrons deflected out of the primary beam region on the detector on the maximum transverse momentum change  $n(|\Delta\mathbf{p}_\perp|)$ . The function  $n(|\Delta\mathbf{p}_\perp|)$  is monotonous and its inverse function  $|\Delta\mathbf{p}_\perp|(n)$  is used to determine the amplitude of the momentum change from the measured number of electrons scattered out of the primary beam region (details are described in the following section).

## 5.4 Numerical simulations

The evolution of electric and magnetic fields in the vicinity of a tungsten nanotip illuminated by a Gaussian pulsed beam with central frequency  $\omega$  and linear polarization perpendicular to the tip surface at the apex (parallel to the tip symmetry axis) is calculated by numerically solving Maxwell's equations using FDTD. Because the relative spectral width of the laser pulses used in the experiments is only  $\Delta\omega/\omega \approx 0.013$ , we calculate the spatial distribution of the complex amplitudes of the near-fields  $\tilde{\mathbf{E}}(\mathbf{r}, \omega)$ ,  $\tilde{\mathbf{B}}(\mathbf{r}, \omega)$  generated at frequency  $\omega$  using the Fourier transform of the time domain field. The simulation region has size of  $5\ \mu\text{m} \times 5\ \mu\text{m} \times 16.235\ \mu\text{m}$  with perfect matching layer at all boundaries. As a source we use a Gaussian beam with the  $1/e^2$  radius of the intensity of  $2.5\ \mu\text{m}$ . We note that the smaller beam size than the one used in the experiments is chosen due to the limitations of the 3D FDTD simulations. However, it does not influence the resulting near-field nor the elastic scattering of the electrons because the interaction is localized on much smaller spatial scales of only a few hundred nanometers. Adaptive mesh with the smallest step of 2 nm is used. The tip is modeled using the radial loft of the bright-field STEM image of the nanotip. The deflection corresponding to each electron trajectory is calculated in the classical approximation by using the trans-

verse momentum change obtained from Eq. (2) with the Lorentz force given by the time-domain fields  $\mathbf{E}(\mathbf{r}, t) = \Re \left\{ \tilde{\mathbf{E}}(\mathbf{r}, \omega) g(t - \Delta t) \exp(i\omega t + i\varphi_0) \right\}$  and  $\mathbf{B}(\mathbf{r}, t) = \Re \left\{ \tilde{\mathbf{B}}(\mathbf{r}, \omega) g(t - \Delta t) \exp(i\omega t + i\varphi_0) \right\}$ .

The electrons are propagated through the calculated electromagnetic fields  $\mathbf{E}(\mathbf{r}, t)$  and  $\mathbf{B}(\mathbf{r}, t)$  using the Monte-Carlo method. The initial electron distribution follows the properties of the electron beam in the experiments. We use normal distribution in time with FWHM duration of 520 fs, homogeneous distribution in the transverse coordinate in the sample plane with the diameter of 21 nm and randomly distributed polar angle in the region 0-1.3 mrad. The 2D histogram of electrons in the detector plane represents the detected scattered image. Function  $n(|\Delta\mathbf{p}_\perp|)$  is obtained by integrating all the electrons scattered out of the region illuminated by the unscattered beam.

## 5.5 Data processing - imaging of the optical standing wave

For data processing, we select only the electrons deflected out of the region illuminated by the unscattered electron beam. The shift of the center of mass of the deflected electron distribution, which is directly proportional to the induced ponderomotive force, is calculated for each position of the beam in the sample plane. The maximum induced momentum change  $\Delta\mathbf{p}_\perp$  is directly obtained from the highest value of the deflection angle of detected electrons (measured from the edge of the primary beam). The intensity of the optical standing wave is calculated using Eq. (2) with the ponderomotive force given by Eq. (4).

## Data availability

All the data that support the plots and the other findings of this study are publicly available at DOI: 10.5281/zenodo.14824588 [53].

## **Code availability**

All the computational codes that were used to generate the data presented in this study are available from the corresponding author upon reasonable request.

## **Author contributions**

M.K. conceived the study. P.K., M.K., K.M. and M.C.Ch.M. performed the experiments and analyzed the data. A.K. and D.B. prepared the nanotips. P.K. and N.L.S. performed the numerical simulations. P.K. and M.K. wrote the manuscript with the contribution from all co-authors.